

# Uncertainty-Aware Decomposed Hybrid Networks

Sina Ditzel<sup>\*1,2</sup>Achref Jaziri<sup>1</sup>Iuliia Plushch<sup>1,3</sup>Visvanathan Ramesh<sup>1</sup><sup>1</sup>Department of Computer Science and Mathematics, Goethe University, 60323 Frankfurt am Main, Germany,<sup>2</sup>Flanders Make, Oude Diestersebaan 133, 3920 Lommel, Belgium<sup>3</sup> Department of Educational Psychology, Goethe University, 60629 Frankfurt am Main, Germany

## Abstract

The robustness of image recognition algorithms remains a critical challenge, as current models often depend on large quantities of labeled data. In this paper, we propose a hybrid approach that combines the adaptability of neural networks with the interpretability, transparency, and robustness of domain-specific quasi-invariant operators. Our method decomposes the recognition into multiple task-specific operators that focus on different characteristics, supported by a novel confidence measurement tailored to these operators. This measurement enables the network to prioritize reliable features and accounts for noise. We argue that our design enhances transparency and robustness, leading to improved performance, particularly in low-data regimes. Experimental results in traffic sign detection highlight the effectiveness of the proposed method, especially in semi-supervised and unsupervised scenarios, underscoring its potential for data-constrained applications.

## 1 INTRODUCTION

Deep neural networks have proven to be highly effective in scenarios where training data sufficiently covers the underlying distribution of the deployment domain. Despite their success, DNNs function as black-box models, limiting interpretability. This opacity can lead to unintended biases, such as reliance on spurious correlations in object placement [Pinto et al., 2008] or biases related to skin tone and gender [Balakrishnan et al., 2020], that are difficult to reveal. Further, this highlights that these models often struggle to generalize to unseen conditions. Real-world applications, however, involve diverse variations, such as changes in pose,

lighting, weather, and sensor quality, which are cumbersome to cover in the dataset. Addressing these challenges requires improving model transparency and robustness. In this work, we propose an approach towards more transparent systems by integrating quasi-invariants, supported explicitly by a confidence measure with neural networks, which we believe can enhance robustness and interpretability.

DNNs implicitly learn transformations for classification without explicitly enforcing invariances [Bengio, 2009, Krizhevsky et al., 2012]. While effective, this lack of explicit control reduces interpretability and increases vulnerability to adversarial attacks [Barredo Arrieta et al., 2020]. To mitigate these issues, research has explored decomposable designs [Lipton, 2016] and targeted specific invariance, typically needed in computer vision applications. Early model-based approaches leveraged quasi-invariant transformations to ensure robustness [Binford and Levitt, 1993, Chin and Dyer, 1986]. Unlike purely data-driven models, quasi-invariant operators offer inherent degree of transparency. The integration of these operators allows for selective suppression of nuisance variables while preserving task-relevant features [Baslamisli et al., 2021]. Hybrid designs, which embed predefined priors as fixed initializations in the first layers of neural networks, have shown improvements in robustness [Dapello et al., 2020, Oyallon et al., 2017]. Recent works [Luan et al., 2018, Jaziri et al., 2024] demonstrate that incorporating quasi-invariant filters, such as Gabor filters and decomposing the input into various parallel streams enhances neural network robustness and representation learning. This also aligns with neuroscience principles, as decomposable vision systems resemble brain-inspired architectures [von der Malsburg, 2014, Hota and Ramesh, 2013]. However, integrating quasi-invariances necessitates complementary uncertainty measures to further refine the decision-making process.

Basic neural networks do not provide confidence estimates and often exhibit over- or under-confidence, leading to miscalibrated predictions. Reliable uncertainty estimates are crucial, particularly in high-risk applications where incor-

<sup>\*</sup>This work was conducted at Goethe university and the time for subsequent writing was supported by Flanders Make.

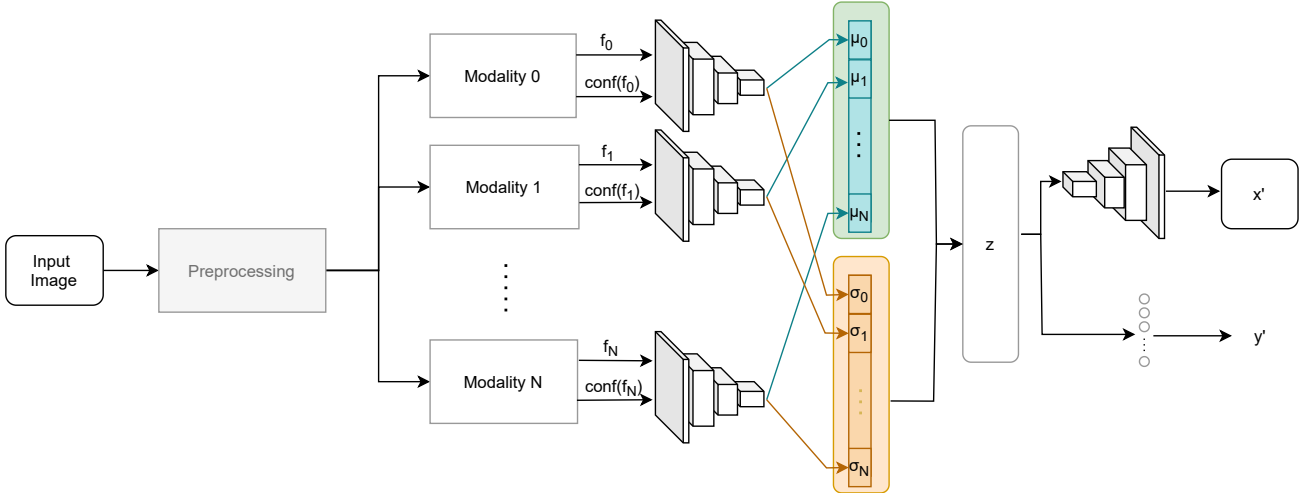


Figure 1: The proposed hybrid architecture decomposes the input image  $x$  using task-specific quasi-invariances  $T_i(x)$ , with computed uncertainties  $\text{conf}(T_i(x))$ . We experimented with different neural architectures that propagate the confidences through initial layers via normalized convolution. The here visualized VAE based architecture encodes the transformed signal into a joint latent space  $z$  (with mean  $\mu$  and standard deviation  $\sigma$ ), which is then used for tasks, such as classification  $y$ .

rect predictions can have serious consequences. Such estimates allow uncertain predictions to be ignored or referred to human experts [Abdar et al., 2021]. Uncertainty estimation is also essential in domains with highly heterogeneous data sources and limited labeled data.

In this work, we illustrate the design of a neural network architecture that leverages inductive biases in the form of known invariance requirements for the task, sensor noise models, decompositions of input data to sub-modalities such as color, texture. We propose a novel confidence measure. Uncertainty modeling and statistical hypotheses tests allow for estimation of posterior probabilities of given sub-modality features that serve as weights in the encoders, producing latent representations in a Variational encoder-decoder architecture formulation (see Figure 1). The task-specific operators are based on invariance properties [Pietikäinen and Zhao, 2015, Gevers and Smeulders, 1999], while the confidence measure builds on prior work in sensor noise modeling [Förstner, 2000, Immerkaer, 1996] and uncertainty propagation through chosen operators [Greiffenhagen et al., 2001]. We leverage normalized convolutions [Eldesokey et al., 2019] to integrate the confidence measure as weight. The design may be seen as a fusion of human devised statistical models and systems analysis along with modern deep learning architectures to enhance transparency, robustness, and explainability of results.

## 2 RELATED WORK

**DNNs with Invariant Operators:** Several studies have explored the integration of well-established operators into data-driven neural networks to enhance transparency and

robustness [Li et al., 2020]. For instance, the SIFT detector, which provides quasi-invariance to scale, orientation, and illumination, has been incorporated into neural architectures to improve feature extraction [Perronnin and Larlus, 2015]. Similarly, adaptations of the Local Binary Pattern operator have been employed to design convolutional layers with reduced parameter complexity, effectively capturing texture features [Juefei-Xu et al., 2017]. Further, Dapello et al. [2020] has shown that simulating the functionality of the primary visual cortex in the early layers of CNNs enhances robustness against input perturbations and adversarial attacks. These methods collectively demonstrate the advantages of integrating structured, interpretable transformations with deep learning models to achieve better robustness and trust. Building on these works, we propose a general framework for decomposable designs incorporating uncertainty estimation of the chosen operators. Our uncertainty aware decomposable design further enhances model reliability and adaptability in diverse application contexts.

**Uncertainty Estimation in Neural Networks:** A key distinction exists between aleatoric uncertainty, which arises from inherent data variability, and epistemic uncertainty, which stems from model limitations [Hacking, 2006]. Aleatoric uncertainty is irreducible, whereas epistemic uncertainty can be minimized with additional training data. Probabilistic methods estimate uncertainty by generating an ensemble of models and quantifying uncertainty through variance or entropy over their predictions [Depeweg et al., 2018]. Deep ensembles [Lakshminarayanan et al., 2017] explicitly train multiple models to capture epistemic uncertainty but are computationally expensive. To mitigate this overhead, alternative approaches approximate deep ensembles without requiring multiple model instances. Recent

works on mode connectivity [Garipov et al., 2018] suggest that ensembles can be optimized along low-loss paths in the weight space, reducing the computational overhead during ensemble training. Bayesian neural networks (BNNs) [MacKay, 1992] employ variational inference [Zhang et al., 2018] to model posterior weight distributions, while Monte-Carlo (MC) dropout [Gal and Ghahramani, 2016] introduces stochasticity through dropout layers to induce variability in predictions. However, these methods come with trade-offs: BNNs incur high runtime costs due to their parameter-heavy nature or can degrade prediction quality. Another line of research explores distribution-free uncertainty estimation using conformal prediction [Balasubramanian et al., 2014] and quantile regression [Angelopoulos et al., 2022] to estimate aleatoric uncertainty bounds. In our approach, aleatoric uncertainty is linked to camera noise, while epistemic uncertainty is managed adaptively within a Bayesian framework by dynamically updating priors.

**Noise Awareness in Model-Based Design:** In traditional computer vision, many studies focus on estimating noise to minimize its effects. Boncelet [2009] reviews noise models and recommendations for mitigation. [Tsin et al., 2001] showed that careful modeling and calibration of the camera response function and its noise sources achieve robust illumination invariant change detection. In other works, sensor noise is often approximated using additive Gaussian Noise, which can be estimated from a single image [Förstner, 2000], with Immerkaer [1996] offering a fast algorithm for this. Gevers and Stokman [2004] and Greiffenhagen et al. [2001] show that propagating the estimated Gaussian noise through color invariant operators improves robustness for recognition systems. Our work is complementary to these approaches as we focus on modeling uncertainty of the chosen operators integrated into data-driven models. We demonstrate how this design paradigm can improve performance, particularly in applications where prior knowledge can inform model structure and uncertainty estimation.

### 3 DECOMPOSED NETWORK WITH CONFIDENCE ESTIMATION

In this section, we introduce a decomposed uncertainty-aware hybrid design illustrated in Figure 1. For each application, different features are relevant, and choosing appropriate (quasi-) invariant transformations is crucial. To stabilize the behavior of these features, we introduce a new confidence measuring approach based on the propagation of input noise.

In the following chapters, we use capital letters (e.g.,  $X$ ) to represent random variables, and small letters (e.g.,  $x$ ) to denote instances and parameters. The hat symbol ( $\hat{X}$  and  $\hat{x}$ ) is used to indicate an observed variable or instance (With noise), and bold letters are used for matrices and vectors. However, we deviate from this convention for  $RGB$ ,  $rg$ , and

$I$  to avoid ambiguity: Image RGB values are represented using capital letters, normalized  $rg$  values use small letters, and intensity  $I$  is also capitalized to differentiate it from indexes  $i$ . Also we use  $N$  to give the number of samples and  $\eta$  is a random variable denoting noise.

#### 3.1 CONFIDENCE OF OPERATORS

To assess the confidence and reliability of image-derived information extracted by an operator, we employ a Bayesian statistical approach that integrates prior knowledge with observed data analysis. Our method incorporates noise modeling, covariance propagation, Mahalanobis distance calculation, and Bayesian likelihood estimation to formulate a novel confidence measure. The approach is based on hypothesis testing, where transformed data from quasi-invariant operators is evaluated against a predefined null hypothesis ( $H_0$ ), representing scenarios where information is deemed less stable or relevant. For instance, in texture and structure based analysis, homogeneous regions may be classified as less significant.

The Bayesian framework provides a probabilistic basis for assessing how well the transformed data fits the model of the null hypothesis, by calculating the confidence  $Conf$  for each value (pixel) as the posterior probability of  $H_0$ , resulting in a confidence map (Figure 2). First we compute the Mahalanobis distance  $d$ , which measures the deviation from the null hypothesis, and then calculate the confidence  $Conf$  for each transformed value based on the observed squared Mahalanobis distance  $\hat{d}^2$ :

$$\begin{aligned} Conf &= P(\neg H_0 | \hat{d}^2) = \\ &= \frac{P(\hat{d}^2 | \neg H_0) P(\neg H_0)}{P(\hat{d}^2 | H_0) P(H_0) + P(\hat{d}^2 | \neg H_0) P(\neg H_0)}. \end{aligned} \quad (1)$$

In cases where prior knowledge is available, this information can be incorporated into the calculation through the prior probabilities  $P(H_0)$  and  $P(\neg H_0)$ . However, if no prior knowledge is available, the formula can be simplified to the likelihood ratio.

##### 3.1.1 Noise Model and Propagation

To calculate the Mahalanobis distance, we need to know the distribution of the data by first modeling the sensor noise and then propagating its covariance through the data transformation process. We adopt a Gaussian noise model for image values, commonly used in image processing to approximate sensor noise due to its simplicity and mathematical properties. Thus we make the assumption, that the noise  $\eta$  affecting the pixel values in a given channel ( $R$ ,  $G$ ,  $B$ , or intensity  $I$ ) follows a Gaussian distribution with mean zero and a channel-specific standard deviation  $\sigma_C$ . For each pixel, the noise is drawn independently from this distribution. Thus, for a true pixel value  $C$ , the observed value  $\hat{C}$  is

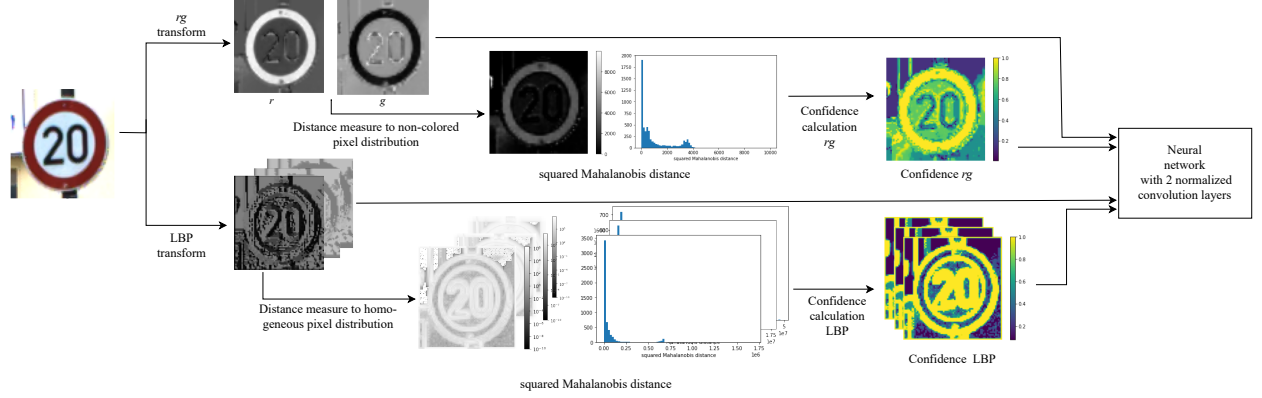


Figure 2: Example of our method applied to the GTSRB dataset using the  $rg$  and LBP operators. The figure shows key intermediate steps, including operator outputs and confidence computation via Mahalanobis distance, calculated per pixel and for visualization also aggregated into a histogram. Both the transformed image and its confidence are propagated through the neural network for a downstream task. Confidence is shown in blue (low) to yellow (high).

modeled as:

$$\hat{C} = C + \eta_C, \quad \eta_C \sim \mathcal{N}(0, \sigma_C^2) \quad (2)$$

We assume the noise distribution can be approximated by deviations in homogeneous regions, using the approach of Shen-Chuan Tai and Shih-Ming Yang [2008]. We then propagate the noise through the operator with linear covariance propagation to estimate the uncertainty of the transformed output, following the approach of Greiffenhagen et al. [2001]. Based on the pre-defined mean  $\mu$  of the null hypothesis  $H_0$ , where the transform is unstable, and using the derived covariance propagation to calculate the covariance matrix  $\Sigma$ , we then calculate the squared Mahalanobis distance  $d^2$  for the transformed values  $\hat{t}$ :

$$d^2(\hat{t}, (\mu, \Sigma)) = (\hat{t} - \mu)^\top \Sigma^{-1} (\hat{t} - \mu). \quad (3)$$

### 3.1.2 Likelihood based on Mahalanobis Distance

We compute the likelihoods  $P(\hat{d}^2 | \neg H_0)$  and  $P(\hat{d}^2 | H_0)$  using the squared Mahalanobis distance  $d^2$ . The probability density functions (PDFs), describing the probability of observing specific values of  $d^2$  under the corresponding hypothesis, are approximated by uniform mixtures of chi-squared distributions and remain consistent across all pixels. The relative likelihood follows from the pixel-specific  $d^2$  value.

The squared Mahalanobis distance  $d^2(X, (\mu, \Sigma))$  of a normal distributed random variable  $X \sim N(\mu, \Sigma)$  follows a  $\chi^2$ -distribution with degrees of freedom equal to the number of dimensions (denoted as  $k$ ) [Johnson and Wichern, 2007, Result 4.7]. Under the defined null hypothesis  $H_0$ , this distribution holds. If  $X$  deviates from  $N(\mu, \Sigma)$  the distribution becomes noncentral  $\chi^2$ , with a noncentrality parameter  $\lambda$  reflecting the deviation. For  $P(\hat{d}^2 | \neg H_0)$  and  $P(\hat{d}^2 | H_0)$  follows:

- Under  $H_0$ :  $d^2$  is  $\chi^2$ -distributed if the Gaussian model holds exactly. In practice, due to noise and approximations, it will follow a mixture of noncentral distributions with small noncentrality.
- Under  $\neg H_0$ :  $d^2$  is a mixture of noncentral  $\chi^2$  distributions, with a higher noncentrality parameter.

In Figure 2, the histogram shows the distribution of the squared Mahalanobis distance for different operators on an example image, where the two peaks correspond to the models for  $H_0$  and  $\neg H_0$ . The peak at 0 aligns with  $H_0$ , while the peak at larger values corresponds to  $\neg H_0$ .

Both PDFs,  $f_{H_0}(x)$  and  $f_{\neg H_0}(x)$ , are approximated using a uniform mixture of noncentral- $\chi^2$ -distribution with noncentrality parameters  $\lambda$  ranging from  $\lambda_1$  to  $\lambda_2$ :

$$f_H(x, \lambda_1, \lambda_2) = \int_{\lambda_1}^{\lambda_2} \frac{1}{\lambda_2 - \lambda_1} f_\chi(x, k, \lambda) d\lambda. \quad (4)$$

For  $H_0$ , this range is chosen to reflect minimal deviation from the central distribution, while for  $\neg H_0$ , the range is set to larger values of  $\lambda$ , capturing the increased deviation under the alternative hypothesis. The exact choice is challenging, thus we compute multiple lambda values and merge the resulting confidence maps. See more details in Appendix C.3. For ease of computation we approximated the uniform mixture of noncentral  $\chi^2$  distributions by a Gaussian distribution based on the first two moments:

$$\mu_H = k + \frac{\lambda_1 + \lambda_2}{2} \quad (5)$$

$$\sigma_H^2 = 2k + 2(\lambda_1 + \lambda_2) + \frac{1}{12}(\lambda_1^2 + 2\lambda_1\lambda_2 + \lambda_2^2). \quad (6)$$

The proof can be found in Appendix A.

### 3.2 USING CONFIDENCE IN NEURAL ENCODER

As highlighted in Figure 1, each operator is paired with an encoder. The encoders outputs are concatenated into a joint latent space, representing the combined information from all operators and serving as input for the downstream tasks. The output of the quasi-invariant transformations along with its confidence map are processed with normalized convolutions [Knutsson and Westin, 1993] in the initial layers of each stream. Feature values are weighted by their confidence scores, reducing the influence of uncertain pixels. This ensures that uncertain regions in the input, have a minimal impact on the output, thereby enhancing the robustness of the learned representations. As by Eldesokey et al. [2019], we combine normalized convolutional layers with confidence pooling. During subsampling, max pooling is applied on confidence values, using the corresponding indices to pool feature maps.

## 4 ADOPTION AND SPECIFICATION FOR TRAFFIC SIGN RECOGNITION

We demonstrate and evaluate our approach on the German Traffic Sign Recognition Benchmark (GTSRB) dataset [Stal Kamp et al., 2012]. Traffic signs exhibit variability in appearance due to changes in illumination, weather conditions, and viewpoints, making them useful for evaluating model invariances and assessing robustness in recognition tasks. Distinctive design features such as shape, color, and symbols (including signs and numbers) make traffic signs highly recognizable. To leverage these properties, we test our methodology using two operators that come with illumination variance: the  $rg$  color transform and Local Binary Patterns (LBP). The  $rg$  transform normalizes color features to reduce illumination effects while retaining critical color information essential for distinguishing traffic signs. LBP captures texture details, encoding crucial shapes and symbols. For each operator, we define a null hypothesis to account for potential feature instability, characterized by its mean  $\mu$  and covariance matrix  $\Sigma$ , which are used to calculate the Mahalanobis distance, based on Equation 3. This distance is then employed to compute a confidence map, based on Equation 1. Below, we provide explanations for each operator. Additional details on the implementations discussed are provided in Appendix C.

### 4.1 COLOR-PROCESSING WITH THE RG-TRANSFORM

The normalized  $rg$  transform is defined as:

$$r = \frac{R}{R + G + B}, \quad g = \frac{G}{R + G + B}. \quad (7)$$

If the illumination is neutral i.e. white light, this model is known to be invariant to shadow, light intensity and light

direction [Gevers and Smeulders, 1999].

Because neutral illumination can not be assumed by default, a correction of the light temperature based on the von Kries model is applied, transforming the recorded color channels to a canonical illuminant through a linear scaling operation. We estimated the illumination using that traffic sign images contains uncolored pixels (i.e., white areas in traffic signs). The deviation from gray, caused by the illuminant's color temperature, is used to approximate the illumination in normalized  $rg$  space. To estimate how the noise changes throughout the  $rg$  transform, Greiffenhagen et al. [Greiffenhagen et al., 2001] have shown that it can be characterized by the following covariance matrix

$$\hat{\Sigma}_{\hat{r}, \hat{g}} \approx \frac{\sigma_I^2}{S^2} \begin{pmatrix} \frac{\sigma_R^2}{\sigma_I^2} (1 - \frac{2R}{S}) + 3\frac{R^2}{S^2} & -\frac{\sigma_G^2 R + \sigma_R^2 G}{\sigma_I^2 S} + 3\frac{RG}{S^2} \\ -\frac{\sigma_G^2 R + \sigma_R^2 G}{\sigma_I^2 S} + 3\frac{RG}{S^2} & \frac{\sigma_G^2}{\sigma_I^2} (1 - \frac{2G}{S}) + 3\frac{G^2}{S^2} \end{pmatrix} \quad (8)$$

with  $S = R + G + B$ ,  $\sigma_I^2 = \frac{\sigma_R^2}{3} = \frac{\sigma_R^2 + \sigma_G^2 + \sigma_B^2}{3}$ .

**Color Confidence Calculation:** Around  $r = g = (\frac{1}{3})$ , where the RGB values are nearly equal, the  $rg$  transform becomes very sensitive to small changes in the RGB values. This sensitivity means that even minor variations or noise in the original RGB values can cause large changes in the  $r$  and  $g$  values. Additionally, this region corresponds to colors close to white or gray, where the color information is less distinct, reducing the transform's ability to extract meaningful features.

Therefore, as confidence measure, we calculate the posterior probability of each pixel not to be close to the point  $r = g = (\frac{1}{3})$ . This is done by testing against the null hypothesis  $H_0$ :

$$H_{0_{rg}} : \text{The pixel is not colored} \\ i.e. \begin{pmatrix} r \\ g \end{pmatrix} = \begin{pmatrix} 1/3 \\ 1/3 \end{pmatrix}. \quad (9)$$

Using the derived covariance matrix  $\Sigma_{\hat{r}, \hat{g}}$  for observed  $rg$  values with noise  $(\hat{r}, \hat{g})^T$  we estimate the distribution of non-colored pixels as:

$$H_{0_{rg}} : \begin{pmatrix} \hat{r} \\ \hat{g} \end{pmatrix} \sim N \left( \begin{pmatrix} 1/3 \\ 1/3 \end{pmatrix}, \Sigma_{\frac{1}{3}, \frac{1}{3}} \right). \quad (10)$$

Where  $\Sigma_{\frac{1}{3}, \frac{1}{3}}$  is approximated by the Equation 8, where  $r = \frac{R}{S} = \frac{1}{3}$ , and  $g = \frac{G}{S} = \frac{1}{3}$  was used.

### 4.2 TEXTURE-PROCESSING WITH LBP

The LBP transform is applied to pixel intensity  $I = \frac{R+G+B}{3}$ . For each pixel value  $I$  a set of neighbors  $I_{n_1}, \dots, I_{n_N}$  is determined based on radius  $r$  and number of points  $p$ . Each neighbor is compared to the center pixel  $I$  in a predefined order along the circle of neighbors. A binary number  $\mathbf{B}$  is generated, where 0 denotes an intensity

lower than the center pixel ( $I_{n_i} - I < 0 \Rightarrow B_i = 0$ ) and 1 otherwise. Converting this binary number to decimal gives the center pixel’s LBP value. For the GTSRB dataset the LBP Operator was used with 3 different sizes. The original parametrization with  $r_1 = 1$ ,  $p_1 = 8$  was complemented by  $r_2 = 2$ ,  $p_2 = 16$  and  $r_3 = 3$ ,  $p_3 = 24$  to cover a variety of scales. All three parametrization have been applied to the intensity of the input image and are subsequently concatenated, to have a three channel input to the CNN.

**LBP Confidence Calculation:** The LBP calculation becomes unstable in homogeneous regions because the noise can switch the sign of the differences. Thus, we calculate the confidence, based on the distance to zero-pixel-difference, i.e. the stronger the difference, the higher is the confidence (that the binary number is correct). This is done by testing against the null hypothesis:

$H_{0_{LBP}}$ : The pixel is in a homogeneous region  
i.e.  $(I_{n_0} - I, I_{n_1} - I, \dots, I_{n_N} - I)^T = (0, 0, \dots, 0)^T$ . (11)

And homogeneous pixels are assumed to be normal distributed:

$$H_{0_{LBP}} : \begin{pmatrix} \hat{I}_{n_0} - \hat{I} \\ \hat{I}_{n_1} - \hat{I} \\ \dots \\ \hat{I}_{n_N} - \hat{I} \end{pmatrix} \sim N \left( \begin{pmatrix} 0 \\ 0 \\ \dots \\ 0 \end{pmatrix}, \Sigma_{LBP} \right). \quad (12)$$

**LBP-Noise Propagation:** The noise is propagated for the differences  $z_i = I_{n_i} - I$ , on which the binary numbers  $B_i$ ’ are based. By calculating the variance and covariance, the following distribution is obtained (detailed variance and covariance derivation can be found in the Appendix B):

$$\Sigma_{LBP} = \begin{pmatrix} 2\sigma^2 & \sigma^2 & \dots & \sigma^2 \\ \sigma^2 & 2\sigma^2 & \dots & \sigma^2 \\ \dots & \dots & \dots & \dots \\ \sigma^2 & \sigma^2 & \dots & 2\sigma^2 \end{pmatrix}. \quad (13)$$

As the variance and covariance is just depending on the noise deviation, which is the same over the whole image (see Section 3.1.1) the covariance matrix  $\Sigma_{LBP}$  is the same for all pixels in one image.

### 4.3 DATASET SPECIFIC PRIORS

We estimated the ratio of pixels of the null hypothesis in the GTSRB dataset by analyzing visual unaltered depictions of the signs. For each pixel, we checked if it belongs to the null hypothesis and the ratio relative to the total number of pixels is calculated, as shown in Figure 3 for some signs.

## 5 EXPERIMENTS

Our empirical investigation follows these key questions:

**Q1) What is the impact of individual quasi-invariant op-**



Figure 3: Visualization of  $H_0$  for a subset of signs: White pixels indicate regions classified under the null hypothesis (non-colored, homogeneous), while black pixels fall outside it. In the boundary area of the sign, half of the pixels are approximated as belonging to the null hypothesis.

**erators with the confidence propagation on classification performance?** We assess the performance of individual quasi-invariant operators (i.e., LBP,  $rg$ ) compared to the baseline CNNs.

**Q2) What is the performance of the decomposed hybrid pipeline?** We explore whether the combination of multiple operators, leads to improved performance or if accuracy is primarily dependent on the strongest individual operator.

**Q3) Does incorporating quasi-invariant operators improve generalization in low-data regimes?** Data-driven models benefit from extensive labeled samples to learn useful features. We hypothesize that by introducing quasi-invariant operators less data is needed to achieve competitive performance. We test this hypothesis by limiting training data to subsets where the maximum number of samples per class in the trainset is limited to 5, 10, 50, and 100.

Before proceeding with the results and analysis, we describe the experimental setup including the training and evaluation approaches, the baselines and the dataset properties. For all experiments, the accuracy of the model on the test set was calculated using the model weights that achieved the highest accuracy on the validation set. All training sessions were repeated 5 times, and the mean and standard deviation of the results are reported. Code is available at: [github.com/SinaDitzel/DecomposedHybridNetworks](https://github.com/SinaDitzel/DecomposedHybridNetworks).

### 5.1 EXPERIMENTAL SETUP

We evaluate three encoder training configurations: supervised, generative, and combination of both. In the supervised setting, the model is trained end-to-end for classification, with a classifier processing concatenated encoder outputs. In the generative setting, a VAE is trained on the dataset in a first step, and the resulting latent representations are used to train a linear classifier with a frozen VAE encoders. We also evaluate a joint optimization of the classifier and traffic sign reconstruction task. We evaluate configurations with and without confidence propagation. When confidence measurements are available, the first two convolutional layers are replaced with normalized convolutional layers. Further details on the neural architectures and hyperparameter settings are provided in Appendix C.5.

		Accuracies on GTSRB dataset		
	Quasi-invariant operator	supervised	generative	both
Baseline (CNN/VAE)	None	<b>98.62</b> $\pm$ 0.41	66.72 $\pm$ 4.44	<b>96.68</b> $\pm$ 0.57
Individual Operators	rg	90.14 $\pm$ 3.67	68.3 $\pm$ 1.56	86.74 $\pm$ 4.09
	rgConf	69.0 $\pm$ 1.74	27.82 $\pm$ 30.05	86.02 $\pm$ 0.39
	LBP	98.0 $\pm$ 0.19	<b>86.76</b> $\pm$ 0.92	<b>96.62</b> $\pm$ 0.24
	LBPCConf	94.92 $\pm$ 0.11	84.46 $\pm$ 1.08	95.32 $\pm$ 0.28
Decomposed Hybrid Systems	rg+LBP	98.16 $\pm$ 0.26	<b>86.38</b> $\pm$ 1.36	<b>96.72</b> $\pm$ 0.19
	rg+LBPCConf	95.82 $\pm$ 0.38	84.08 $\pm$ 2.09	95.76 $\pm$ 0.11
	rgConf+LBP	98.12 $\pm$ 0.18	<b>86.34</b> $\pm$ 0.73	<b>96.64</b> $\pm$ 0.21
	rgConf+LBPCConf	94.44 $\pm$ 0.59	84.3 $\pm$ 2.05	95.68 $\pm$ 0.59

Table 1: Results on the GTSRB dataset: accuracies of different operator(rg or LBP) combinations with and without confidence propagation(Conf). Mean accuracies are **bolded** if they are the highest or within the 95% confidence interval of the highest.

		Accuracys on <b>clustered</b> GTSRB dataset		
	Quasi-invariant operator	supervised	generative	both
Baseline (CNN/VAE)	None	<b>99.6</b> $\pm$ 0.07	91.44 $\pm$ 1.84	98.88 $\pm$ 0.28
Individual Operators	rg	98.9 $\pm$ 0.12	97.32 $\pm$ 0.38	98.54 $\pm$ 0.25
	rgConf	97.92 $\pm$ 0.49	54.92 $\pm$ 22.41	98.52 $\pm$ 0.23
	LBP	99.56 $\pm$ 0.15	97.76 $\pm$ 0.54	98.82 $\pm$ 0.42
	LBPCConf	98.46 $\pm$ 0.31	97.24 $\pm$ 0.38	98.56 $\pm$ 0.18
Decomposed Hybrid Systems	rg+LBP	<b>99.52</b> $\pm$ 0.08	<b>98.58</b> $\pm$ 0.15	<b>99.28</b> $\pm$ 0.08
	rg+LBPCConf	99.36 $\pm$ 0.44	97.64 $\pm$ 0.85	99.0 $\pm$ 0.12
	rgConf+LBP	<b>99.62</b> $\pm$ 0.11	98.2 $\pm$ 0.22	<b>99.32</b> $\pm$ 0.19
	rgConf+LBPCConf	99.16 $\pm$ 0.23	97.26 $\pm$ 0.15	98.98 $\pm$ 0.16

Table 2: Results on the clustered-GTSRB dataset, where classes with the same color and shape are merged, showing the accuracies in the same structure as the full GTSRB dataset.

The dataset was split into training and test sets using the pre-defined GTSRB splits [Stallkamp et al., 2012]. A validation set was created by separating 15% of the training samples, with non-random sampling to avoid overlap, ensuring at least 10% of each class came from complete tracks.

## 5.2 RESULTS AND DISCUSSION

**(Q1) LBP is most suitable operator for the traffic sign domain:** Table 1 presents classification accuracies across different settings. In the supervised setting, the CNN has the highest mean accuracy, while the decomposed model demonstrates competitive performance, maintaining accuracy close to the baseline CNN with lower variance across runs. Among the operators, LBP consistently performed well across all configurations, often matching or surpassing the baseline, particularly in generative training. In contrast, the *rg* transform demonstrated lower performance, partic-

ularly in confidence propagation. This can be attributed to its reliance on color information, which is not always a distinctive feature in GTSRB, where many classes share similar color patterns. These findings suggest that color information alone is insufficient for robust street sign classification. Specifically, confidence propagation assigns low confidence to discriminative, non-color-based features in the image, leading to performance degradation. To further investigate this, we evaluated the system on a clustered dataset, where the 43 original classes were grouped into 7 clusters based on color and shape. As shown in Table 2, the *rg* transform performed significantly better in this setting, confirming that our *rg*-encoder effectively captures color-based features when they are more discriminative. These results highlight the importance of leveraging complementary modalities to achieve competitive performance across diverse domains while also obtaining more disentangled representations, thereby enhancing transparency.



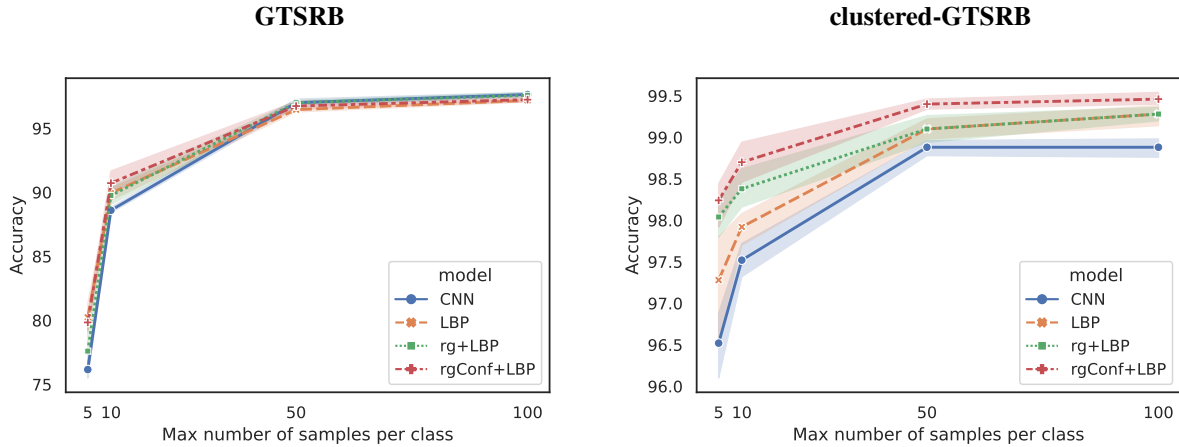


Figure 4: Classification results in a supervised setting in the limited sample setting on the GTSRB and clustered-GTSRB dataset.

**(Q2) A decomposed multi-stream design improves the performance:** Our system integrates multiple complementary features by combining operators that focus on specific modalities. The results indicate that combining parallel encoders with different modalities consistently improves performance. While LBP performs well in supervised and semi-supervised settings, its performance further improves when combined with the *rg* operator. A decomposed hybrid design combining both *rg* and LBP achieves the best overall performance in most cases. However, in the supervised case on the non-clustered GTSRB dataset, the CNN outperforms it, highlighting the effectiveness of fully data-driven learning on large dataset. Among the decomposed hybrid systems, we see that the combination of *rg*, confidence propagation, and LBP yields high accuracies. Particularly on the clustered dataset where this combination has the highest mean accuracy in the supervised and semi-supervised setting. However, when both operators were combined with confidence propagation, performance slightly declined, likely due to excessive suppression of discriminative information. This highlights the need to balance invariance induction and feature retention to maximize system effectiveness.

**(Q3) The decomposed design outperforms the baseline in low-sample-setting** Figure 4 visualizes the most effective operator combinations from previous experiments across different sample sizes. Corresponding tables are provided in Appendix D.1. Our decomposed hybrid network *rgConf+LBP* consistently outperforms the baseline CNN, demonstrating superior performance retention in low-data settings due to its introduced invariance.

While traditional image processing operators such as LBP have proven effective, they are seldom integrated into modern deep learning frameworks. Our results indicate that incorporating such model-based operators can significantly enhance performance. The proposed confidence measure is

most effective when the selected modality provides clear class distinctions. Furthermore, our findings highlight that the performance of the decomposed hybrid system improves with stronger operator selection. When appropriately chosen, these operators enable the model to surpass the baseline CNN, particularly in data-limited scenarios, underscoring the importance of structured feature extraction in deep learning architectures.

## 6 CONCLUSION

In this work, we explored decomposed hybrid encoder designs, combining quasi invariant operators with neural networks. We introduced a novel confidence measurement leveraging noise estimation, covariance propagation, and hypothesis testing, allowing networks to prioritize features with high confidence during encoding. Evaluations on the GTSRB demonstrated the impact of task-appropriate quasi-invariant operators and their complementary effects. Notably, LBP proved to be a strong inductive bias for traffic sign recognition, and a hybrid network integrating the *rg* operator, confidence measurement, and LBP achieved competitive performance, outperforming the baseline CNN in the unsupervised and the low-data settings. These findings highlight the advantages of integrating well understood operators along with their uncertainty estimates into data-driven models. Future work should extend this framework to new domains by incorporating additional quasi-invariant operators and explore full uncertainty propagation across network representations and final classifications.

## Acknowledgements

The authors acknowledge the support of various sponsors that made this research possible. This work was supported



by the German Federal Ministry of Education and Research (BMBF) funded projects 01IS19062 "AISEL".

Further for providing time to collaboratively write and finalize the work, Achref Jaziri was supported by the project 45KI16E051 "KIBA" (Künstliche Intelligenz und diskrete Beladeoptimierungsmodelle zur Auslastungssteigerung im kombinierten Verkehr), Iuliia Pluiisch was supported by 16DHBKI019 "ALI", and S. Ditzel acknowledges the support of Flanders Make (<https://www.flandersmake.be>), the strategic research center for the manufacturing industry, and the Flanders AI Research Program (<https://www.flandersairesearch.be>).

## References

- Moloud Abdar, Farhad Pourpanah, Sadiq Hussain, Dana Rezadegan, Li Liu, Mohammad Ghavamzadeh, Paul Fieguth, Xiaochun Cao, Abbas Khosravi, U Rajendra Acharya, et al. A review of uncertainty quantification in deep learning: Techniques, applications and challenges. *Information fusion*, 76:243–297, 2021.
- Anastasios N Angelopoulos, Amit Pal Kohli, Stephen Bates, Michael Jordan, Jitendra Malik, Thayer Alshaabi, Srigokul Upadhyayula, and Yaniv Romano. Image-to-image regression with distribution-free uncertainty quantification and applications in imaging. In *International Conference on Machine Learning*, pages 717–730. PMLR, 2022.
- Guha Balakrishnan, Yuanjun Xiong, Wei Xia, and Pietro Perona. Towards Causal Benchmarking of Bias in Face Analysis Algorithms. In *European Conference on Computer Vision (ECCV)*, pages 547–563, 2020. ISBN 9783030585228. doi: 10.1007/978-3-030-58523-5\_32. URL [https://doi.org/10.1007/978-3-030-58523-5\\_32](https://doi.org/10.1007/978-3-030-58523-5_32).
- Vineeth Balasubramanian, Shen-Shyang Ho, and Vladimir Vovk. *Conformal prediction for reliable machine learning: theory, adaptations and applications*. Newnes, 2014.
- Alejandro Barredo Arrieta, Natalia Díaz-Rodríguez, Javier Del Ser, Adrien Bannetot, Siham Tabik, Alberto Barabado, Salvador Garcia, Sergio Gil-Lopez, Daniel Molina, Richard Benjamins, Raja Chatila, and Francisco Herrera. Explainable Artificial Intelligence (XAI): Concepts, taxonomies, opportunities and challenges toward responsible AI. *Information Fusion*, 58:82–115, 2020. ISSN 15662535. doi: 10.1016/j.inffus.2019.12.012. URL <https://doi.org/10.1016/j.inffus.2019.12.012>.
- Anil S. Baslamisli, Yang Liu, Sezer Karaoglu, and Theo Gevers. Physics-based shading reconstruction for intrinsic image decomposition. *Computer Vision and Image Understanding*, 205, 2021. ISSN 1090235X. doi: 10.1016/j.cviu.2021.103183.
- Yoshua Bengio. Learning deep architectures for ai. *Foundations and Trends® in Machine Learning*, 2(1):1–127, 2009.
- Thomas O Binford and Tod S Levitt. Quasi-invariants: Theory and exploitation. In *Proc. DARPA Image Understanding Workshop*, pages 819–829, 1993.
- Charles Bonchelet. Image noise models. In *The essential guide to image processing*, pages 143–167. Elsevier, 2009.
- Roland T Chin and Charles R Dyer. Model-based recognition in robot vision. *ACM Computing Surveys (CSUR)*, 18(1):67–108, 1986.
- Joel Dapello, Tiago Marques, Martin Schrimpf, Franziska Geiger, David Cox, and James J DiCarlo. Simulating a primary visual cortex at the front of cnns improves robustness to image perturbations. *Advances in Neural Information Processing Systems*, 33:13073–13087, 2020.
- Stefan Depeweg, Jose-Miguel Hernandez-Lobato, Finale Doshi-Velez, and Steffen Udluft. Decomposition of uncertainty in bayesian deep learning for efficient and risk-sensitive learning. In *International conference on machine learning*, pages 1184–1193. PMLR, 2018.
- Abdelrahman Eldesokey, Michael Felsberg, and Fahad Shahbaz Khan. Confidence propagation through cnns for guided sparse depth regression. *IEEE transactions on pattern analysis and machine intelligence*, 2019.
- Wolfgang Förstner. Image preprocessing for feature extraction in digital intensity, color and range images. In *Geomatic method for the analysis of data in the earth sciences*, pages 165–189. Springer, 2000.
- Yarin Gal and Zoubin Ghahramani. Dropout as a bayesian approximation: Representing model uncertainty in deep learning. In *international conference on machine learning*, pages 1050–1059. PMLR, 2016.
- Timur Garipov, Pavel Izmailov, Dmitrii Podoprikin, Dmitry P Vetrov, and Andrew G Wilson. Loss surfaces, mode connectivity, and fast ensembling of dnns. *Advances in neural information processing systems*, 31, 2018.
- Theo Gevers and Arnold WM Smeulders. Color-based object recognition. *Pattern recognition*, 32(3):453–464, 1999.
- Theo Gevers and Harro Stokman. Robust histogram construction from color invariants for object recognition. *IEEE transactions on pattern analysis and machine intelligence*, 26(1):113–118, 2004.

- M. Greiffenhagen, D. Comaniciu, H. Niemann, and V. Ramesh. Design, analysis, and engineering of video monitoring systems: an approach and a case study. *Proceedings of the IEEE*, 89(10):1498–1517, 2001.
- Ian Hacking. *The emergence of probability: A philosophical study of early ideas about probability, induction and statistical inference*. Cambridge University Press, 2006.
- Kaiming He, Xiangyu Zhang, Shaoqing Ren, and Jian Sun. Delving deep into rectifiers: Surpassing human-level performance on imagenet classification. In *Proceedings of the IEEE international conference on computer vision*, pages 1026–1034, 2015.
- R. Hota and V. Ramesh. Video surveillance – case study for cognitive vision. Bernstein Conference 2013, 2013. doi: 10.12751/nncn.bc2013.0196.
- John Immerkaer. Fast noise variance estimation. *Computer vision and image understanding*, 64(2):300–302, 1996.
- Achref Jaziri, Sina Ditzel, Iuliia Pliushch, and Visvanathan Ramesh. Representation learning in a decomposed encoder design for bio-inspired hebbian learning. In *Proceedings of the European Conference on Computer Vision Workshops*, 2024.
- R. A. Johnson and D. W. Wichern. *Applied Multivariate Statistical Analysis*. Pearson, 6th edition, 2007.
- Felix Juefei-Xu, Vishnu Naresh Boddeti, and Marios Savvides. Local binary convolutional neural networks. In *Proceedings of the Computer Vision and Pattern Recognition Conference (CVPR)*, pages 19–28, 2017.
- F. Jurišić, I. Filković, and Z. Kalafatić. Multiple-dataset traffic sign classification with onecnn. In *2015 3rd IAPR Asian Conference on Pattern Recognition (ACPR)*, pages 614–618, 2015. doi: 10.1109/ACPR.2015.7486576.
- Hans Knutsson and C-F Westin. Normalized and differential convolution. In *Proceedings of IEEE Conference on Computer Vision and Pattern Recognition*, pages 515–523. IEEE, 1993.
- Alex Krizhevsky, Ilya Sutskever, and Geoffrey E Hinton. Imagenet classification with deep convolutional neural networks. In *Advances in Neural Information Processing Systems (NeurIPS)*, volume 25, 2012.
- Balaji Lakshminarayanan, Alexander Pritzel, and Charles Blundell. Simple and scalable predictive uncertainty estimation using deep ensembles. *Advances in neural information processing systems*, 30, 2017.
- Qiufu Li, Linlin Shen, Sheng Guo, and Zhihui Lai. Wavelet integrated cnns for noise-robust image classification. In *Proceedings of the Computer Vision and Pattern Recognition Conference (CVPR)*, pages 7245–7254, 2020.
- Zachary C Lipton. The mythos of model interpretability. In *ICML Workshop on Human Interpretability in Machine Learning*, 2016.
- Shangzhen Luan, Chen Chen, Baochang Zhang, Jungong Han, and Jianzhuang Liu. Gabor convolutional networks. *IEEE Transactions on Image Processing*, 27(9):4357–4366, 2018. ISSN 10577149. doi: 10.1109/TIP.2018.2835143.
- David JC MacKay. A practical bayesian framework for backpropagation networks. *Neural computation*, 4(3): 448–472, 1992.
- E. Oyallon, E. Belilovsky, and S. Zagoruyko. Scaling the scattering transform: Deep hybrid networks. In *2017 IEEE International Conference on Computer Vision (ICCV)*, pages 5619–5628, 2017.
- Florent Perronnin and Diane Larlus. Fisher vectors meet neural networks: A hybrid classification architecture. In *Proceedings of the Computer Vision and Pattern Recognition Conference (CVPR)*, pages 3743–3752, 2015.
- Matti Pietikäinen and Guoying Zhao. Two decades of local binary patterns: A survey. In *Advances in independent component analysis and learning machines*, pages 175–210. Elsevier, 2015.
- Nicolas Pinto, David D. Cox, and James J. DiCarlo. Why is real-world visual object recognition hard? *PLoS Computational Biology*, 4:333 – 341, 2008.
- Shen-Chuan Tai and Shih-Ming Yang. A fast method for image noise estimation using laplacian operator and adaptive edge detection. In *2008 3rd International Symposium on Communications, Control and Signal Processing*, pages 1077–1081, 2008. doi: 10.1109/ISCCSP.2008.4537384.
- Johannes Stalkamp, Marc Schlipsing, Jan Salmen, and Christian Igel. Man vs. computer: Benchmarking machine learning algorithms for traffic sign recognition. *Neural networks*, 32:323–332, 2012.
- Yanghai Tsin, Visvanathan Ramesh, and Takeo Kanade. Statistical calibration of ccd imaging process. In *Proceedings Eighth IEEE International Conference on Computer Vision. ICCV 2001*, volume 1, pages 480–487. IEEE, 2001.
- Christoph von der Malsburg. A vision architecture. *arXiv preprint arXiv:1407.1642*, 2014.
- J. von Kries. Influence of adaptation on the effects produced by luminous stimuli. In D. L. MacAdam, editor, *Sources of Color Vision*, 61:109–119, 1970.
- Jun yan Huo, Yi lin Chang, Jing Wang, and Xiao xia Wei. Robust automatic white balance algorithm using gray color points in images. *IEEE Transactions on Consumer Electronics*, 52(2):541–546, 2006. doi: 10.1109/TCE.2006.1649677.

Cheng Zhang, Judith Bütepage, Hedvig Kjellström, and  
Stephan Mandt. Advances in variational inference. *IEEE  
transactions on pattern analysis and machine intelligence*,  
41(8):2008–2026, 2018.

---

# Uncertainty-Aware Decomposed Hybrid Networks (Supplementary Material)

---

Sina Ditzel<sup>\*1,2</sup>

Achref Jaziri<sup>1</sup>

Iuliia Pliushch<sup>1,3</sup>

Visvanathan Ramesh<sup>1</sup>

<sup>1</sup>Department of Computer Science and Mathematics, Goethe University, 60323 Frankfurt am Main, Germany,

<sup>2</sup>Flanders Make, Oude Diestersebaan 133, 3920 Lommel, Belgium

<sup>3</sup> Department of Educational Psychology, Goethe University, 60629 Frankfurt am Main, Germany

## A DERIVATION OF THE APPROXIMATION OF THE MIXTURE OF $\chi^2$ DISTRIBUTIONS

As we explained in the main body, for ease of the computation we approximate the uniform mixture of  $\chi^2$  distributions by its first two moments. In this section we offer the derivation of these moments.

To reinstate, we defined the pdf  $f_{a,b}(x)$  of a uniform mixture of noncentral  $\chi^2$  distributions with pdf  $f_\chi(x, k, \lambda)$  over a certain range  $[a, b]$  as

$$f_{a,b}(x) = \int_a^b \frac{1}{b-a} f_\chi(x, k, \lambda) d\lambda. \quad (14)$$

In the following proof we will use the expected value and variance of a noncentral- $\chi^2$  distributed variable  $X_\chi$  with the probability density function  $f_\chi(x, k, \lambda)$ . The expectation and variance are:

$$E[X_\chi] = \int_{-\infty}^{\infty} x f_\chi(x, k, \lambda) dx = k + \lambda, \quad (15)$$

$$\begin{aligned} Var[X_\chi] &= \int_{-\infty}^{\infty} (x - E[X_\chi])^2 f_\chi(x, k, \lambda) dx \\ &= 2(k + 2\lambda). \end{aligned} \quad (16)$$

For the uniform mixture of noncentral- $\chi^2$  distribution, we will first show the derivation of the expectation. For a random variable  $X$ , with pdf  $f_{a,b}(x)$  the expectation  $E[X]$  is:

$$\begin{aligned} E[X] &\stackrel{28}{=} \int_{-\infty}^{\infty} x f_{a,b}(x) dx \\ &= \int_{-\infty}^{\infty} x \int_a^b \frac{1}{b-a} f_\chi(x, k, \lambda) d\lambda dx \\ &= \frac{1}{b-a} \int_a^b \int_{-\infty}^{\infty} x f_\chi(x, k, \lambda) dx d\lambda \\ &\stackrel{15}{=} \frac{1}{b-a} \int_a^b (k + \lambda) d\lambda \\ &= \frac{1}{b-a} \left[ k\lambda + \frac{\lambda^2}{2} \right]_{\lambda=a}^{\lambda=b} \end{aligned} \quad (17)$$

---

<sup>\*</sup>This work was conducted at Goethe university and the time for subsequent writing was supported by Flanders Make.

<sup>\*</sup>This work was conducted at Goethe university and the time for subsequent writing was supported by Flanders Make.

$$= \frac{(kb + \frac{b^2}{2} - ka - \frac{a^2}{2})}{b-a} = k + \frac{a+b}{2}. \quad (18)$$

Next, we will calculate the variance of  $X$ . Therefore, we show first that the variance can be transformed to three terms, by expanding the squared parenthesis and multiply all sub-terms with  $f_{a,b}(x)$ :

$$\begin{aligned} Var[X] &\stackrel{29}{=} \int_{-\infty}^{\infty} (x - E[X])^2 f_{a,b}(x) dx \\ &= \int_{-\infty}^{\infty} (x^2 - 2xE[X] + E[X]^2) f_{a,b}(x) dx \\ &= \int_{-\infty}^{\infty} x^2 f_{a,b}(x) - 2xE[X] f_{a,b}(x) + E[X]^2 f_{a,b}(x) dx \\ &= \underbrace{\int_{-\infty}^{\infty} x^2 f_{a,b}(x) dx}_{\text{see 21}} - \underbrace{\int_{-\infty}^{\infty} 2xE[X] f_{a,b}(x) dx}_{\text{see 22}} \\ &\quad + \underbrace{\int_{-\infty}^{\infty} E[X]^2 f_{a,b}(x) dx}_{\text{see 23}}. \end{aligned} \quad (19)$$

The first term can be expand to three terms, by adding  $0 = -2x(k + \lambda) + (k + \lambda)^2 + 2x(k + \lambda) - (k + \lambda)^2$  to  $x^2$ :

$$\begin{aligned} x^2 &= x^2 - 2x(k + \lambda) + (k + \lambda)^2 + 2x(k + \lambda) - (k + \lambda)^2 \\ &= ((x - (k + \lambda))^2 + 2x(k + \lambda) - (k + \lambda)^2). \end{aligned} \quad (20)$$

This allows us to rewrite the formula to contain the formulas for  $E[X_\chi]$  and  $Var[X_\chi]$  and an integral over a pdf that sums to 1, to simplify the formula, that we can then integrate.

$$\begin{aligned} \int_{-\infty}^{\infty} x^2 f_{a,b}(x) dx &= \int_{-\infty}^{\infty} x^2 \int_a^b \frac{1}{b-a} f_\chi(x, k, \lambda) d\lambda dx \\ &= \frac{1}{b-a} \int_a^b \int_{-\infty}^{\infty} x^2 f_\chi(x, k, \lambda) dx d\lambda \\ &\stackrel{20}{=} \frac{1}{b-a} \int_a^b \underbrace{\int_{-\infty}^{\infty} (x - (k + \lambda))^2 f_\chi(x, k, \lambda) dx}_{\stackrel{16}{=} 2(k+2\lambda)} d\lambda + \frac{2}{b-a} \int_a^b (k + \lambda) \underbrace{\int_{-\infty}^{\infty} x f_\chi(x, k, \lambda) dx}_{\stackrel{15}{=} k+\lambda} d\lambda \\ &\quad - \frac{1}{b-a} \int_a^b (k + \lambda)^2 \underbrace{\int_{-\infty}^{\infty} f_\chi(x, k, \lambda) dx}_{=1} d\lambda \\ &= \frac{1}{b-a} \int_a^b 2(k + 2\lambda) d\lambda + \frac{2}{b-a} \int_a^b (k + \lambda)^2 d\lambda - \frac{1}{b-a} \int_a^b (k + \lambda)^2 d\lambda \\ &= \frac{2}{b-a} \int_a^b k + 2\lambda d\lambda + \frac{1}{b-a} \int_a^b (k + \lambda)^2 d\lambda \\ &= \frac{2}{b-a} [k\lambda + \lambda^2]_{\lambda=a}^{\lambda=b} + \frac{1}{b-a} [k^2\lambda + k\lambda^2 + 1/3\lambda^3]_{\lambda=a}^{\lambda=b} \\ &= \frac{2kb - 2ka + 2b^2 - 2a^2}{b-a} + \frac{k^2b - k^2a + kb^2 - ka^2 + \frac{1}{3}b^3 - \frac{1}{3}a^3}{b-a} \\ &= \frac{(2k + k^2)b - (2k + k^2)a + (2 + k)b^2 - (2 + k)a^2}{b-a} + \frac{\frac{1}{3}b^3 - \frac{1}{3}a^3}{b-a} \\ &= \frac{(2k + k^2)(b-a)}{b-a} + \frac{(2 + k)(b^2 - a^2)}{b-a} \frac{(\frac{1}{3})(b^3 - a^3)}{b-a} \end{aligned}$$

$$=(2k + k^2) + (2 + k)(a + b) + \frac{1}{3}(a^2 + ab + b^2). \quad (21)$$

The second term we can move the constant outside the integral, so that only the expectation  $E[X]$  remains in the integral:

$$\begin{aligned} \int_{-\infty}^{\infty} 2xE[X]f_{a,b}(x)dx &= \int_{-\infty}^{\infty} 2xE[X] \int_a^b \frac{1}{b-a} f_{\chi}(x, k, \lambda) d\lambda dx \\ &= 2E[X] \int_{-\infty}^{\infty} x \int_a^b \frac{1}{b-a} f_{\chi}(x, k, \lambda) d\lambda dx \\ &= 2E[X]E[X] \\ &= 2E[X]^2. \end{aligned} \quad (22)$$

In the third term, we can use again that a integral over all possible outcomes of a pdf sums up to 1, such that

$$\int_{-\infty}^{\infty} E[X]^2 f_{a,b}(x)dx = E[X]^2 \int_{-\infty}^{\infty} f_{a,b}(x)dx = E[X]^2. \quad (23)$$

Combining the transformations, we then gain the short equation for the variance, presented in the main paper:

$$\begin{aligned} \text{Var}[X] &= \underbrace{\int_{-\infty}^{\infty} x^2 f_{a,b}(x)dx}_{\text{see 21}} - \underbrace{\int_{-\infty}^{\infty} 2xE[X]f_{a,b}(x)dx}_{\text{see 22}} + \underbrace{\int_{-\infty}^{\infty} E[X]^2 f_{a,b}(x)dx}_{\text{see 23}} \\ &= (2k + k^2) + (2 + k)(a + b) + \frac{1}{3}(a^2 + ab + b^2) - 2E[X]^2 + E[X]^2 \\ &= 2k + k^2 + (2 + k)(a + b) + \frac{1}{3}(a^2 + ab + b^2) - \left(k + \frac{a+b}{2}\right)^2 \\ &= 2k + 2(a + b) + \frac{1}{3}(a^2 + ab + b^2) - \frac{1}{4}(a^2 + 2ab + b^2) \\ &= 2k + 2(a + b) + \frac{1}{12}(a^2 + 2ab + b^2). \end{aligned} \quad (24)$$

## B VARIANCE AND COVARIANCE OF LBP DISTRIBUTION

In the main paper, we chose LBP as one of the quasi-invariances to use. For its computation, intensity  $I$  is first computed from the RGB value, from which distance  $z_i = I_{n_i} - I$  is computed to the neighboring pixel intensities  $I_{n_i}$ . In order to compute the confidence that these distances  $\mathbf{z}$  are relevant, we chose zero-centered Gaussian noise as our intensity noise model:  $\hat{I} = I + \eta$  with  $\eta \sim \mathcal{N}(0, \sigma^2)$ .

Hence, the random variable  $\hat{Z}_i$  (from which we observe  $\hat{z}_i$ ) can be expressed as:

$$\hat{Z}_i = \hat{I}_{n_i} - \hat{I} = (I_{n_i} + \eta_i) - (I + \eta). \quad (25)$$

In the main paper we stated the covariance matrix for these distances, which we will derive here. As a covariance matrix is a square matrix that encapsulates the variances and covariances, we will derive  $\text{Var}[\hat{Z}_i]$  and  $\text{Cov}[\hat{Z}_i, \hat{Z}_j]$  for pixel  $\hat{Z}_i$  and neighbour  $\hat{Z}_j$ .

### B.1 DEFINITIONS AND FORMULAS FOR VARIANCE AND EXPECTATION

First, we provide definitions and formulas for variance and expectation, which are basic concepts in probability theory and statistics, and which we will use in the following sections.



The variance of a random variable  $X$  is a measure of how much the values of  $X$  vary from its expected value. The variance is denoted by  $\text{Var}[X]$  and is defined as

$$\text{Var}[X] = E[(X - E[X])^2]. \quad (26)$$

where  $E[X]$  is the expected value of  $X$ .

The covariance between two random variables  $X$  and  $Y$  is a measure of how much the two variables vary together. The covariance is denoted by  $\text{Cov}[X, Y]$  and is defined as

$$\text{Cov}[X, Y] = E[(X - E[X])(Y - E[Y])]. \quad (27)$$

For a continuous variable  $X$  with pdf  $f(x)$  the expectation is defined as

$$E[X] = \int_{-\infty}^{\infty} x f(x) \, dx. \quad (28)$$

and the variance can be calculated with

$$\text{Var}[X] = \int_{-\infty}^{\infty} (x - E[X])^2 f(x) \, dx. \quad (29)$$

## B.2 VARIANCE

$$\begin{aligned} \text{Var}[\hat{Z}_i] &= \text{Var}[(\hat{I}_{n_i} - \hat{I})^2] \\ &= \text{Var}[\hat{I}_{n_i}] + \text{Var}[\hat{I}] - 2\text{Cov}[\hat{I}_{n_i}, \hat{I}] \\ &= \text{Var}[\hat{I}_{n_i}] + \text{Var}[\hat{I}] \\ &= 2\sigma^2. \end{aligned} \quad (30)$$

## B.3 COVARIANCE

Next we compute the covariance between two distances (of the center pixel to two different neighbors). We will use that the difference between the variable of the distance  $\hat{Z}_i$  to its expected value  $z_i$  can be expressed as the difference between the noise terms:

$$\begin{aligned} \hat{Z}_i - z_i &= (I_{n_i} + \eta_i - (I + \eta)) - (I_{n_i} - I) \\ &= \eta_i - \eta. \end{aligned} \quad (31)$$

We calculate the covariance as

$$\begin{aligned} \text{Cov}[\hat{Z}_i, \hat{Z}_j] &= E[(\hat{Z}_i - z_i)(\hat{Z}_j - z_j)] \\ &= E[(\eta_i - \eta)(\eta_j - \eta)] \\ &= E[\eta_i \eta_j] + E[\eta_i(-\eta)] + E[\eta_j(-\eta)] + E[\eta^2] \\ &= 0 + 0 + 0 + \sigma^2 = \sigma^2. \end{aligned} \quad (32)$$

This holds due to the relationship between the noise factors:  $E[\eta_i \eta_j] = E[\eta_i \eta] = E[\eta_j \eta] = 0$ , as  $\eta_i \eta_j \eta$  are independent:

$$\begin{aligned} E[\eta_i \eta_j] &= E[((I_{n_i} + \eta_i) - I_{n_i})((I_{n_j} + \eta_j) - I_{n_j})] \\ &= \text{Cov}[\hat{I}_{n_i}, \hat{I}_{n_j}] = 0, \end{aligned} \quad (33)$$

and  $E[\eta \eta] = \sigma^2$ :

$$\begin{aligned} E[\eta \eta] &= E[((I + \eta) - I)^2] \\ &= \text{Var}[\hat{I}] = \sigma^2. \end{aligned} \quad (34)$$

## C FURTHER IMPLEMENTATION DETAILS

In this section, we provide additional information on the implementation of our method, including details on the noise estimation, illumination correction, setting appropriate  $\lambda$  values, and calculating priors. Further, we detail the architecture and hyperparameters of the neural network.

### C.1 NOISE ESTIMATION

As mentioned in the main body we assume the noise distribution can be approximated by deviations in homogeneous region. We implemented a noise estimation method[Shen-Chuan Tai and Shih-Ming Yang, 2008], which first uses the Sobel operator for edge detection to detect areas with less structure, then a Laplacian operator is additionally applied which suppresses image structures, so that the residuals can be used to calculate the standard deviation. We used the 10% of the area with the least structure. Additionally, 5% of pixels with the highest and lowest intensity and saturation have also been discarded for more stability. A Canny-edge detector was used with thresholds  $t_1 = 55\%$  and  $t_2 = 75\%$ , the neighborhood size  $n_s$  has been set to 5 pixels.

### C.2 ILLUMINATION CORRECTION

Before we use the  $rg$ -transform we first apply a illumination correction, to achieve (more) neutral illumination. Based on the von Kries Model[von Kries, 1970] the image  $(R_{e'}, G_{e'}, B_{e'})^T$  taken under an unknown light illumination  $e' = (e'_R, e'_G, e'_B)^T$  can be transformed to image  $(R_e, G_e, B_e)^T$  taken under the canonical illuminant  $e$  by linear transformation, that independently scales the three recorded color channels:

$$\begin{pmatrix} R_e \\ G_e \\ B_e \end{pmatrix} = \begin{pmatrix} \frac{e_R}{e'_R} & 0 & 0 \\ 0 & \frac{e_G}{e'_G} & 0 \\ 0 & 0 & \frac{e_B}{e'_B} \end{pmatrix} \begin{pmatrix} R_{e'} \\ G_{e'} \\ B_{e'} \end{pmatrix}. \quad (35)$$

The illumination  $e'$  is estimated based on the assumption, that an image consists of numerous gray ( $R = G = B$ ) pixels. Especially for street signs this assumption holds because every sign consists of white areas. In the image taken under illumination  $e'$  these gray values might be slightly shifted. The deviation, introduced by the color temperature of the illuminant, is used to approximate  $e'$ , similar to [yan Huo et al., 2006]. In the normalized  $rg$  space all gray values ( $R = G = B$ ) are given by  $\mathbf{rg} = (\frac{1}{3}, \frac{1}{3})^T$ . Thus, for each color channel the mean  $\bar{r}$  and  $\bar{g}$  of values in a specified range  $\delta$  around the gray point  $[\frac{1}{3} - \delta, \frac{1}{3} + \delta]$  is calculated, and assumed to be the light color in  $rg$  space. Leading to the following illumination correction:

$$\begin{pmatrix} r \\ g \end{pmatrix} = \begin{pmatrix} \frac{1/3}{\bar{r}} & 0 & 0 \\ 0 & \frac{1/3}{\bar{g}} & 0 \end{pmatrix} \begin{pmatrix} r' \\ g' \end{pmatrix}. \quad (36)$$

### C.3 SETTING $\lambda$ VALUES

In the main body, we explained that we approximate  $H_0$  and  $\neg H_0$  by a uniform mixture of noncentral- $\chi^2$ -distribution with noncentrality parameters  $\lambda$  ranging from  $\lambda_1$  to  $\lambda_2$ . For  $H_0$  we set  $\lambda$  to range from  $\lambda_{2_{H_0}} = 0$  (representing small deviations from centrality) to  $\lambda_{2_{H_0}}$ . For  $\neg H_0$ , the noncentrality parameter starts from  $\lambda_{2_{H_0}}$ , such that  $\lambda_{2_{H_0}} = \lambda_{1_{\neg H_0}}$ , indicating a clear departure from centrality. Selecting appropriate values for  $\lambda_{2_{H_0}} = \lambda_{1_{\neg H_0}}$  and  $\lambda_{2_{\neg H_0}}$  is challenging, as deviation from the mean depends on the conditions under which the images were captured. To address this, we compute multiple  $\lambda$  values per image, including one adaptive value based on the distribution of Mahalanobis distances ( $\hat{d}$ ).

Collecting all  $\hat{d}$  for an image into the vector  $\hat{\mathbf{d}}$ , we choose  $\lambda_{2_{H_0}} = \lambda_{1_{\neg H_0}}$  values as 0, 100, 1000,  $\frac{1}{2} \text{median}(\hat{\mathbf{d}})$  and compute a weighted mean from the resulting confidence maps. To capture high deviations  $\lambda_{2_{\neg H_0}}$  is set to  $1.75 \cdot \text{median}(\hat{\mathbf{d}})$ .

### C.4 PRIOR CALCULATION

We estimated the ratio of pixels belonging to the null hypothesis in the GTSRB dataset. To analyze the ratio, we use visual (unaltered) depictions of the signs instead of recorded images. We check for each pixel of the sign if it belonging to the null hypothesis and calculated the ratio of those to the total number of pixels. We assume all pixels with  $r = \frac{1}{3}$  and  $g = \frac{1}{3}$  as not

colored and all pixels with no difference to the neighbors  $\text{sum}(z_0, \dots, z_N) = 0$  as homogeneous according to the definitions of null hypothesis Equation 9 and Equation 11. For the boundary area around the sign, which is unknown, we approximate an equal distribution of pixels belonging to the null hypothesis  $P(H_0)=50\%$ . This leads to the masks visualized in Figure 3 for a subset of the signs. We average those over all signs to calculate the priors, which leads to  $P(H_{0_{rg}}) = 47.2\%$  and  $P(H_{0_{LBP_{1,8}}}) = 54.45\%$ ,  $P(H_{0_{LBP_{3,24}}}) = 52.2\%$ ,  $P(H_{0_{LBP_{5,40}}}) = 50.36\%$  on the GTSRB dataset.

## C.5 NEURAL ARCHITECTURES

Each operator is paired with an encoder, and we evaluated three different model configurations: supervised CNN, generative VAE, and combination of both. The supervised setting involves a multilayer perceptron (MLP) that takes the (concatenated) outputs of the encoders as input. In the semi-supervised configuration, we optimize both the MLP and the reconstruction of the traffic signs, leveraging the latent representations learned by the encoders. In the generative setting, a VAE is trained on the dataset in a first step, and the resulting latent representations are used to train a linear classifier with a frozen VAE encoders. We evaluate different combinations with and without confidence propagation. In scenarios where the input data includes confidence measurements, the first two convolutional layers of all architectures are replaced with normalized convolutional layers[Eldesokey et al., 2019]. Additionally, confidence pooling is applied during subsampling. The CNN architecture is adapted from OneCNN [Jurišić et al., 2015], their architecture achieved over 99% on the GTSRB dataset. Our adaptation preserves the same number of layers and kernel sizes but excluding skip connections. We also used a patch size of  $48 \times 48$  and a batch size of 64, consistent with the settings in OneCNN [Jurišić et al., 2015]. The VAE architecture consists of an encoder with 5 convolutional layers and a decoder with 5 transposed convolutional layers. The input size for the VAE is set to  $128 \times 128$  to enable more effective feature reconstruction. Training is performed using the Adam optimizer with a learning rate of  $10^{-3}$  for 50 epochs, and the Kaiming weight initialization[He et al., 2015] is applied for improved convergence. The model architectures are described in Table 3.

Architecture	Layer Type	Details
CNN	Convolution	64 channels, 5x5 kernel, stride 1, no padding
	Max-Pooling	2x2 window, stride 2
	Convolution	128 channels, 3x3 kernel, stride 1, no padding
	Max-Pooling	2x2 window, stride 2
	Convolution	128 channels, 3x3 kernel, stride 1, no padding
	Max-Pooling	2x2 window, stride 2
VAE Encoder	Convolution	128 channels, 3x3 kernel, stride 2, padding 1
	Convolution	256 channels, 3x3 kernel, stride 2, padding 1
	Convolution	512 channels, 3x3 kernel, stride 2, padding 1
	Convolution	1024 channels, 3x3 kernel, stride 2, padding 1
	Latent Space	Outputs $\mu$ and $\sigma$ for $z$ with dimension 128.
VAE Decoder	Transposed Convolution	512 channels, 3x3 kernel, stride 2, padding 1
	Transposed Convolution	256 channels, 3x3 kernel, stride 2, padding 1
	Transposed Convolution	128 channels, 3x3 kernel, stride 2, padding 1
	Transposed Convolution	3 channels, 3x3 kernel, stride 2, padding 1
MLP Classifier	Dropout	Probability 0.25
	Linear	Input: classifier_input_dim, Output: 128
	Linear	Non-linearity
	Dropout	Probability 0.25
	Linear	Input: 128, Output: num_classes

Table 3: Summary of CNN, VAE, and MLP Classifier Architectures. Convolutional layers (and equivalent for transposed convolution layers) for the supervised and semi-supervised training are followed by Batch Normalization and ReLU activation. In the pre-trained VAE only ReLU activation without Batch Normalization is used. In the VAE Encoder, the final layer computes  $\mu$  and  $\sigma$  for the latent variable  $z$  with dimension 128. In scenarios where the input data includes confidence measurements, the first two convolutional layers of all architectures are replaced with normalized convolutional layers and the first two poolings with confidence pooling

## D FURTHER EXPERIMENTAL RESULTS

### D.1 LIMITED SAMPLE SETTING

In Table 4 are some more detailed results on the GTSRB dataset for the limited sample setting described in the main body. Figure 5 visualize how the dataset is clustered for the experiments on the clustered dataset and Table 5 shows the detailed result for the clustered dataset.

Method	#samples=5	#samples=10	#samples=50	#samples=100
CNN	76.16 $\pm$ 0.79	88.6 $\pm$ 0.25	97.0 $\pm$ 0.37	97.64 $\pm$ 0.21
rg	53.2 $\pm$ 1.73	62.96 $\pm$ 1.07	84.26 $\pm$ 0.67	88.3 $\pm$ 0.38
rgConf	42.36 $\pm$ 0.86	44.94 $\pm$ 0.94	52.66 $\pm$ 0.66	55.72 $\pm$ 0.87
LBP	80.24 $\pm$ 1.49	89.94 $\pm$ 0.61	96.46 $\pm$ 0.23	97.18 $\pm$ 0.16
LBPCConf	66.28 $\pm$ 1.9	75.42 $\pm$ 0.76	86.68 $\pm$ 0.89	89.22 $\pm$ 0.46
rg+LBP	77.6 $\pm$ 2.12	89.76 $\pm$ 0.9	97.0 $\pm$ 0.21	97.58 $\pm$ 0.23
rg+LBPCConf	65.5 $\pm$ 2.46	76.44 $\pm$ 1.68	90.44 $\pm$ 0.78	92.9 $\pm$ 0.47
rgConf+LBP	79.84 $\pm$ 0.76	90.72 $\pm$ 1.05	96.74 $\pm$ 0.38	97.24 $\pm$ 0.21
rgConf+LBPCConf	68.82 $\pm$ 1.91	76.38 $\pm$ 0.47	87.72 $\pm$ 0.94	89.86 $\pm$ 0.44

Table 4: Accuracies where the maximum number of samples per class is limited to  $p = 5, 10, 50, 100$  on the GTSRB dataset

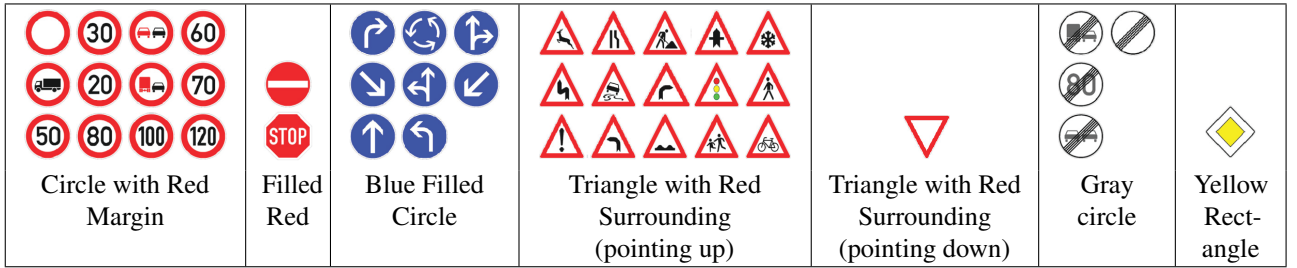


Figure 5: Classes of the clustered GTSRB dataset

Method	#samples=5	#samples=10	#samples=50	#samples=100
CNN	96.52 $\pm$ 0.5	97.52 $\pm$ 0.26	98.88 $\pm$ 0.11	98.88 $\pm$ 0.13
rg	96.02 $\pm$ 0.3	96.22 $\pm$ 0.55	97.94 $\pm$ 0.23	98.28 $\pm$ 0.13
rgConf	93.0 $\pm$ 0.6	94.56 $\pm$ 0.88	96.52 $\pm$ 0.22	97.16 $\pm$ 0.21
LBP	97.28 $\pm$ 0.75	97.92 $\pm$ 0.25	99.1 $\pm$ 0.16	99.28 $\pm$ 0.16
LBPCConf	90.84 $\pm$ 0.41	93.68 $\pm$ 0.64	96.5 $\pm$ 0.23	97.12 $\pm$ 0.18
rg+LBP	98.04 $\pm$ 0.3	98.38 $\pm$ 0.3	99.1 $\pm$ 0.2	99.28 $\pm$ 0.11
rg+LBPCConf	97.12 $\pm$ 0.25	97.38 $\pm$ 0.38	98.5 $\pm$ 0.14	99.02 $\pm$ 0.08
rgConf+LBP	98.24 $\pm$ 0.36	98.7 $\pm$ 0.28	99.4 $\pm$ 0.07	99.46 $\pm$ 0.09
rgConf+LBPCConf	96.2 $\pm$ 0.46	96.92 $\pm$ 0.43	98.46 $\pm$ 0.22	98.94 $\pm$ 0.11

Table 5: Accuracies where the maximum number of samples per class is limited to  $p = 5, 10, 50, 100$  on the **clustered** GTSRB dataset